Stresses at grain boundaries

The maximum incompatibility stress in an infinitely extended elastic bicrystal under uniaxial loading

Liu, Kai; Sluiter, Marcel H.F.

DOI
10.1016/j.scriptamat.2023.115570

Publication date
2023

Document Version
Final published version

Published in
Scripta Materialia

Scripta Materialia 234 (2023) 115570

Contents lists available at ScienceDirect

Scripta Materialia

journal homepage: www.journals.elsevier.com/scripta-materialia

Stresses at grain boundaries: The maximum incompatibility stress in an infinitely extended elastic bicrystal under uniaxial loading

Kai Liu [a,*], Marcel H.F. Sluiter [a,b,*]

[a] Department of Materials Science and Engineering, Delft University of Technology, Mekelweg 2, Delft, 2628 CD, the Netherlands
[b] Department of Electromechanical, Systems and Metal Engineering, Faculty of Engineering and Architecture, Ghent University (UGent), Technologiepark 46, Zwijnaarde, B-9052, Belgium

ARTICLE INFO

MSC:
74A50

Keywords:
Grain boundary
Incompatibility stress
Anisotropy
Texture
Orientation

ABSTRACT

In a material under stress, grain boundaries may give rise to stress discontinuities. Stress localization is crucial to materials' behavior such as segregation, precipitation, and void nucleation. Here, the stress state at a grain boundary perpendicular to a uniaxial external stress is studied systematically. The grain boundary with the most extreme stress discontinuity is determined for cubic materials within the elastic limit for a bicrystal model. Additionally, grain boundaries with negligible stress discontinuity are identified. The influence of the elastic tensor components, C_{11}, C_{12}, and C_{44}, and grain orientation is studied quantitatively.

Grain boundaries (GBs) act as walls that divide the bulk into parts with different orientations and discontinuous tensorial properties. Under loading, the misorientation of grains and the intrinsic anisotropy of the crystal lead to a stress discontinuity at the GBs, resulting in stress states that deviate significantly from the average. The stress discontinuity at GBs strongly influences some phenomena at the grain scale, such as grain growth [1,2] and segregation [3]. Moreover, since the failure of materials is controlled by extreme values of localized stresses rather than by the average stress level in the material, the stress discontinuity at certain GBs strongly affects materials' mechanical behavior, such as crack initiation under loading [4], fatigue [5–7], corrosion cracking [8], and creep [9–11]. Grain boundary engineering [12] and new manufacturing methods show great promise for optimizing material performance through control of texture [13,14] and GB structure [15]. Therefore, investigating how stress states at GBs are influenced by grain orientations can help design polycrystalline materials with optimized textures [16].

Theoretically, already three decades ago, certain special GBs, such as the tilt symmetrical GB and twist GB [17–19], were studied and analytic solutions for those particular incompatibility stresses (IS) were derived. A few years ago, for bicrystals, an explicit closed-form solution for IS for general GBs was derived and verified through finite element method (FEM) simulations [20]. This solution was then applied to study the stress state at $\Sigma 3\langle 1\ \ 1\ \ 1\rangle$ twin boundaries [21] and the activation of dislocations in nickel bicrystalline micropillars [22]. It was revealed that IS plays a crucial role in activating slip, which directly affects the plastic deformation of metals. For polycrystals, FEM simulations and statistical analysis have shown that the inclination angle of grain boundaries, grain size, and triple junctions have a significant influence on IS [23–26].

In addition to IS at GBs, there are several theoretical studies on the interaction of dislocations with GBs. The elastic field induced by dislocations [36] and the dislocation pile-ups behavior [35,36] near GBs in anisotropic materials are strongly affected by the orientations of the grains.

Previous works either focus on special cases, which are not guaranteed to find the stress build-up extrema [17–19], or focus on polycrystals, which yield many details but do not easily reveal general rules about specific GBs [23–26].

This work starts from a bicrystal model with an external stress σ^{E} perpendicular to the GB, aiming to identify the extrema of the IS and to gain insight into the stress state. We derive an analytical solution for the extreme value of the IS at the GB in terms of the elastic tensor components. It is revealed that the GB with the highest IS is the same for all cubic materials. Furthermore, the magnitude of IS for general GBs under perpendicular uniaxial applied stress is quantitatively described.

* Corresponding authors.
E-mail addresses: k.liu-3@tudelft.nl (K. Liu), m.h.f.sluiter@tudelft.nl (M.H.F. Sluiter).

https://doi.org/10.1016/j.scriptamat.2023.115570
Received 25 November 2022; Received in revised form 8 May 2023; Accepted 15 May 2023
Available online 24 May 2023

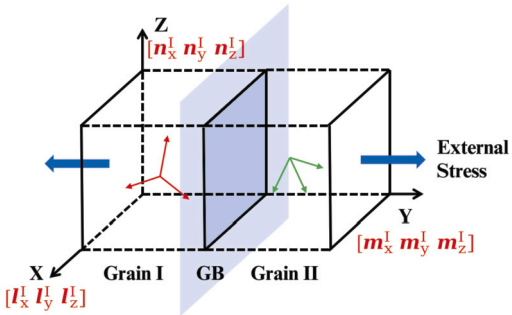

Fig. 1. (Color online) The schematic figure of the bicrystal model in this work. The size of the GB in the X and Z direction is infinite. The two grains are semi-infinite. The orientation of each grain is represented by three Miller indices. The blue arrows show the uniaxial external stress σ^E applied far from the GB, which is perpendicular to GB plane. The label of the grain is shown at the superscript.

The bicrystal model applied in this study is shown in Fig. 1. The 3-dimensional space is divided into two semi-infinite half-spaces separated by the GB. In keeping consistency with previous work [21], the GB plane is fixed parallel to the global XOZ plane, and the direction of σ^E is set along the global Y-axis, perpendicular to the GB. We firstly focus on the stress state near GBs that are perpendicular to σ^E. Experiments [27] and simulations [25] suggest that GBs perpendicular to σ^E are more likely to be the initial site of failure.

Two grains with the same material property but with different orientations are labeled as grain I and grain II. For cubic materials, the orientations of crystals can be conveniently described with Miller indices. For grain I,

$$\hat{e}^I = \begin{bmatrix} l_x^I & l_y^I & l_z^I \\ m_x^I & m_y^I & m_z^I \\ n_x^I & n_y^I & n_z^I \end{bmatrix}, \tag{1}$$

where $\boldsymbol{l}^I$, $\boldsymbol{m}^I$, $\boldsymbol{n}^I$ are normalized Miller indices of the crystallographic orientation of grain I corresponding to X, Y, and Z-axis in global coordinate system, respectively. Then the orientation of grain I is uniquely represented with $[l_x^I \;\; l_y^I \;\; l_z^I]$ and $[m_x^I \;\; m_y^I \;\; m_z^I]$, and analogously for grain II.

The compliance tensor $\boldsymbol{S'}$ after rotation $\hat{e}$, is given by

$$\boldsymbol{S}'_{mnop} = \hat{e}_{mi}\hat{e}_{nj}\hat{e}_{ok}\hat{e}_{pl}\boldsymbol{S}_{ijkl}, \tag{2}$$

in which $\boldsymbol{S}$ is the compliance tensor in the cubic crystal coordinate system.

Within the continuum description of GBs the following constraints apply for the bicrystal model.

1. The two grains are rigidly glued together at the GB. No relative motion is allowed at the GB.
2. The model contains only one GB with infinite size. The interaction between GBs is not included.
3. The model is valid within the linear elastic limit.
4. σ^E is along global Y-axis, which is perpendicular to the GB plane.

Considering the equilibrium equations for momentum, the stress field in the bicrystal model must be invariant with respect to the Y coordinate. The discontinuity of a scalar field $g(x_i)$ at the GB is represented as $[g] = g^I - g^{II}$ then IS can be presented as $[\sigma_{ij}]$.

The constitutive equation of a linear elastic material is

$$\varepsilon_{ij} = S_{ijkl}\sigma_{kl}. \tag{3}$$

According to the first constraint listed above, strain components in the GB plane are continuous,

$$[\varepsilon_{ij}] = 0, \quad i,j = 1,3. \tag{4}$$

Since σ^E is a far-field stress, global stress equilibrium requires

$$\frac{1}{V}\int_V \sigma_{ij}dV = \Sigma_{ij}, \tag{5}$$

where Σ_{ij} is the general external stress [20]. In this problem Σ_{ij} only contains σ^E. So

$$\begin{cases} \sigma_{22}^I = \sigma_{22}^{II} = \sigma^E \\ \sigma_{23}^I = \sigma_{23}^{II} = 0 \\ \sigma_{12}^I = \sigma_{12}^{II} = 0 \end{cases}. \tag{6}$$

Since the model assumes that each grain occupies half the space, Eq. (5) is equivalent to

$$\Sigma_{ij} = \frac{1}{2}(\sigma_{ij}^I + \sigma_{ij}^{II}). \tag{7}$$

Then for in-plane stress components can be written as

$$\sigma_{ij}^I + \sigma_{ij}^{II} = 0, \quad i,j = 1,3. \tag{8}$$

According to Eq. (6), the stress states at both sides of the GB are

$$\begin{cases} \sigma^I = [\sigma_1, \sigma^E, \sigma_3, 0, \sigma_5, 0] \\ \sigma^{II} = [-\sigma_1, \sigma^E, -\sigma_3, 0, -\sigma_5, 0], \end{cases} \tag{9}$$

with Voigt notation (xx → 1, yy → 2, zz → 3, yz → 4, xz → 5, xy → 6). Noticing σ_4 and σ_6 are zero, the global Y-axis is one of the principal directions for the stress state. When the global coordinate system is rotated around its Y-axis, the in-plane stress components can be represented by a Mohr circle. Then $(\sigma_1 + \sigma_3)$ is an invariant for $[\sigma_{ij}]$ during the rotation.

Consider the discontinuity of hydrostatic stress σ_h at the GB,

$$[\sigma_h] = \frac{2(\sigma_1 + \sigma_3)}{3}. \tag{10}$$

As our description is in the linear elastic limit, all stresses are proportional to σ^E. Therefore it is convenient to define an incompatibility factor (IF) as

$$IF = \frac{\sigma_1 + \sigma_3}{\sigma^E}. \tag{11}$$

When exchanging the labeling of the two grains, IF changes sign, so that only the absolute value of IF has physical meaning. Then σ_h at either side of GB can be expressed as

$$\sigma_h = \frac{(1 \pm IF)\sigma^E}{3} \tag{12}$$

In Supplement A a Python module is provided for computing IF analytically.

Hayes and Shuvalov proposed a parameter χ to characterize the Young's modulus anisotropy of cubic crystals [28],

$$\chi = 2s_{11} - 2s_{12} - s_{44}. \tag{13}$$

Here s_{ij} refers to compliance components written with Voigt notation and with the engineering convention ($s_{44} = 4s_{yzyz} = 4s_{xyxy} = 4s_{xzxz}$). Here we derive a property of 4th rank tensors of cubic crystals using Voigt notation, with special application to the compliance matrix. The compliance matrix after rotation is given as (see Supplement B for details)

$$\boldsymbol{S'} = \boldsymbol{S} + \chi \boldsymbol{F}(\boldsymbol{l}, \boldsymbol{m}, \boldsymbol{n}), \tag{14}$$

where $\boldsymbol{F}$ is a 6 by 6 symmetric matrix of polynomials of $\boldsymbol{l}, \boldsymbol{m}, \boldsymbol{n}$ components, e.g.

$$F_{22} = -(m_x^2 m_y^2 + m_x^2 m_z^2 + m_y^2 m_z^2), \tag{15}$$

$$F_{25} = m_x^2 l_x n_x + m_y^2 l_y n_y + m_z^2 l_z n_z, \tag{16}$$

$$F_{55} = -4(n_x n_y l_x l_y + n_x n_z l_x l_z + n_y n_z l_y l_z). \tag{17}$$

Since $\boldsymbol{F}$ doesn't contain any elastic tensor components, it is common for all cubic materials.

For two grains with compliance tensor S^{I} and S^{II} it is convenient to properly rotate the coordinate system along Y axis to make $\sigma_1 = \sigma_3$. According to Eq. (3), (9), and (14), the strain continuity equation (Eq. (4)) can be recast as

$$\begin{cases} [(F^{\mathrm{I}}_{11}+F^{\mathrm{II}}_{11})\chi+2s_{11}+(F^{\mathrm{I}}_{13}+F^{\mathrm{II}}_{13})\chi+2s_{12}]\sigma_1+(F^{\mathrm{I}}_{12}-F^{\mathrm{II}}_{12})\chi\sigma^{\mathrm{E}}+(F^{\mathrm{I}}_{15}+F^{\mathrm{II}}_{15})\chi\sigma_5=0, \\ [(F^{\mathrm{I}}_{33}+F^{\mathrm{II}}_{33})\chi+2s_{11}+(F^{\mathrm{I}}_{31}+F^{\mathrm{II}}_{31})\chi+2s_{12}]\sigma_1+(F^{\mathrm{I}}_{32}-F^{\mathrm{II}}_{32})\chi\sigma^{\mathrm{E}}+(F^{\mathrm{I}}_{35}+F^{\mathrm{II}}_{35})\chi\sigma_5=0, \\ (F^{\mathrm{I}}_{51}+F^{\mathrm{II}}_{51}+F^{\mathrm{I}}_{53}+F^{\mathrm{II}}_{53})\chi\sigma_1+(F^{\mathrm{I}}_{52}-F^{\mathrm{II}}_{52})\chi\sigma^{\mathrm{E}}+[(F^{\mathrm{I}}_{55}+F^{\mathrm{II}}_{55})\chi+2s_{44}]\sigma_5=0. \end{cases} \tag{18}$$

Then considering the orthonormality of $\boldsymbol{l}$, $\boldsymbol{m}$, and $\boldsymbol{n}$ of $\hat{\boldsymbol{e}}$, the expression for σ_1 is simplified as

$$\frac{\sigma_1}{\sigma^{\mathrm{E}}} = \frac{(F^{\mathrm{I}}_{22}-F^{\mathrm{II}}_{22})[(F^{\mathrm{I}}_{55}+F^{\mathrm{II}}_{55})\chi+2s_{44}]\chi-[(F^{\mathrm{I}}_{25})^2-(F^{\mathrm{II}}_{25})^2]\chi^2}{[(F^{\mathrm{I}}_{22}+F^{\mathrm{II}}_{22})\chi+4s_{11}+4s_{12}][(F^{\mathrm{I}}_{55}+F^{\mathrm{II}}_{55})\chi+2s_{44}]-(F^{\mathrm{I}}_{25}+F^{\mathrm{II}}_{25})^2\chi^2}. \tag{19}$$

Considering a global coordinate system rotated around Y-axis such that $\sigma_1 = \sigma_3$, it follows that

$$IF = \frac{2\sigma_1}{\sigma^{\mathrm{E}}}. \tag{20}$$

Then, Eq. (19) shows the orientation dependence of σ_1 as well as of IF. Referring to Eq. (15), (16), and (17), for each grain, we can consider F_{22} as reflecting the effects of two degrees of freedom of the grain rotation, while F_{25} contains the remaining 1 degree of freedom, which represents the rotation of the grain around the Y-axis. Considering the connection between Young's modulus of the grain along the global Y-axis and compliance components, as

$$E_{\mathrm{Y}} = \frac{1}{S'_{22}} = \frac{1}{F_{22}\chi+s_{11}}, \tag{21}$$

terms with F_{22} show the influence of the stiffness of the grain along the global Y-axis. Eq. (19) fits well with our intuition about the IS. Intuitively, one might link the IS to the difference of transverse strain (induced by the Poisson effect) across the GB. A grain with a low (high) Young's modulus along the loading direction has a large (small) positive longitudinal elastic strain, which leads to a large (small) negative transverse strain in the GB plane. Thus the IF is related to the discontinuity of the Young's modulus along the Y-axis.

According to Eq. (15), the range of F_{22} is estimated as

$$F_{22} = -(m_{\mathrm{x}}^2 m_{\mathrm{y}}^2 + m_{\mathrm{x}}^2 m_{\mathrm{z}}^2 + m_{\mathrm{y}}^2 m_{\mathrm{z}}^2) = \frac{m_{\mathrm{x}}^4 + m_{\mathrm{y}}^4 + m_{\mathrm{z}}^4 - 1}{2}. \tag{22}$$

The maximum (minimum) of F_{22} is 0 ($-\frac{1}{3}$) when $\boldsymbol{m}$ is along $\langle 1\ \ 0\ \ 0\rangle$ ($\langle 1\ \ 1\ \ 1\rangle$). For F_{55}, Eq. (17) can be written as

$$F_{55} = -4(n_{\mathrm{x}}n_{\mathrm{y}}l_{\mathrm{x}}l_{\mathrm{y}} + n_{\mathrm{x}}n_{\mathrm{z}}l_{\mathrm{x}}l_{\mathrm{z}} + n_{\mathrm{y}}n_{\mathrm{z}}l_{\mathrm{y}}l_{\mathrm{z}}) = 2(l_{\mathrm{x}}^2 n_{\mathrm{x}}^2 + l_{\mathrm{y}}^2 n_{\mathrm{y}}^2 + l_{\mathrm{z}}^2 n_{\mathrm{z}}^2). \tag{23}$$

The maximum (minimum) of F_{55} is 1 (0) when $\boldsymbol{l}$, $\boldsymbol{n}$ are along $\langle 1\ \ 1\ \ 0\rangle$ and $\langle -1\ \ 1\ \ 0\rangle$ ($\langle 1\ \ 0\ \ 0\rangle$ and $\langle 0\ \ 1\ \ 1\rangle$), $\boldsymbol{l}$ and $\boldsymbol{n}$ can be exchanged.

The value of F_{25} is found numerically, which gives a maximum of $\frac{1}{4}$ when $\boldsymbol{l}$, $\boldsymbol{m}$ are along $\langle 1\ \ -1\ \ \sqrt{2}\rangle$ and $\langle 1\ \ 1\ \ 0\rangle$ (in arbitrary order), respectively. When exchanging the sequence of $\boldsymbol{l}$ and $\boldsymbol{n}$, F_{25} changes its sign. F_{25} approaches 0 when F_{22} approaches its extrema.

It's difficult to derive the extreme value of $\sigma_1/\sigma^{\mathrm{E}}$ mathematically since Eq. (19) contains both rotation variables and material elastic components. The following two points are considered to search for the maximum $\sigma_1/\sigma^{\mathrm{E}}$.

1. F_{25} is much less than 1, and it appears quadratically only. This shows that the influence of the rotation of the grain around the Y-axis is relatively small.
2. When F_{22} approaches its extremum, i.e. $F_{22} = 0$ and $F_{22} = -\frac{1}{3}$, terms with F_{25} vanish.

Then the expression of $\sigma_1/\sigma^{\mathrm{E}}$ simplifies to

$$\begin{aligned} \frac{\sigma_1}{\sigma^{\mathrm{E}}} &\approx \frac{(F^{\mathrm{I}}_{22}-F^{\mathrm{II}}_{22})[(F^{\mathrm{I}}_{55}+F^{\mathrm{II}}_{55})\chi+2s_{44}]\chi}{[(F^{\mathrm{I}}_{22}+F^{\mathrm{II}}_{22})\chi+4s_{11}+4s_{12}][(F^{\mathrm{I}}_{55}+F^{\mathrm{II}}_{55})\chi+2s_{44}]} \\ &= \frac{(F^{\mathrm{I}}_{22}-F^{\mathrm{II}}_{22})\chi}{[(F^{\mathrm{I}}_{22}+F^{\mathrm{II}}_{22})\chi+4s_{11}+4s_{12}]}. \end{aligned} \tag{24}$$

For $\chi > 0$ ($\chi < 0$), the maximum (minimum) for Eq. (24) is achieved when $F^{\mathrm{I}}_{22} = 0$ and $F^{\mathrm{II}}_{22} = -\frac{1}{3}$, which corresponds to $\boldsymbol{m}^{I}$ and $\boldsymbol{m}^{\mathrm{II}}$ parallel to $\langle 1\ \ 0\ \ 0\rangle$ and $\langle 1\ \ 1\ \ 1\rangle$, respectively. With Eq. (11) and (24), and $\sigma_1 = \sigma_3$, the maximum value of IF is

$$\begin{aligned} IF^{\max} &= \frac{2\chi/3}{-\chi/3+4s_{11}+4s_{12}} \\ &= \frac{4s_{11}-4s_{12}-2s_{44}}{10s_{11}+14s_{12}+s_{44}} \\ &= \frac{-2\left(C_{11}-C_{12}-2C_{44}\right)\left(C_{11}+2C_{12}\right)}{\left(10C_{11}-4C_{12}\right)C_{44}+\left(C_{11}-C_{12}\right)\left(C_{11}+2C_{12}\right)}. \end{aligned} \tag{25}$$

After conducting large-scale sampling of IF for the bicrystal model with various grain orientations, it is confirmed that Eq. (25) represents the global maximum of IF.

We found the magnitude of IF is related to the elastic instability of cubic crystals. The elastic stability conditions for cubic crystals are

$$C_{11}-C_{12} > 0,\quad C_{11}+2C_{12} > 0,\quad C_{44} > 0, \tag{26}$$

or, equivalently

$$-\frac{1}{2} < \frac{C_{12}}{C_{11}} < 1,\quad \frac{C_{44}}{C_{11}} > 0. \tag{27}$$

The $IF^{\max}$ values, as computed with Eq. (25), for common metals are shown in Fig. 2(a) using the experimentally determined elastic tensor components [29]. When C_{12}/C_{11} approaches 1, or C_{44}/C_{11} approaches 0, which means the stability of the crystal is low according to Eq. (27), the absolute value of $IF^{\max}$ rises rapidly.

In alloys the $IF^{\max}$ can be designed on purpose. The types and concentrations of alloying elements can influence the elastic properties of alloys as has been shown experimentally and computationally [30,31]. By designing alloys with low $IF^{\max}$ using Fig. 2(a), it might be possible to improve properties that are sensitive to the stress state at GBs.

At the GB, not only the discontinuities in stresses are of interest, but large values of local stresses themselves are of importance too. Therefore, the σ_{h} values on both sides of the GB corresponding to $IF^{\max}$ are calculated. The stress concentration factor F_{h} is defined as the ratio of the σ_{h} values on both sides of the GB to the value of the hydrostatic stress without a GB under σ^{E},

$$F_{\mathrm{h}} = \frac{3\sigma_{\mathrm{h}}}{\sigma^{\mathrm{E}}} = 1 \pm IF. \tag{28}$$

The most extreme F_{h} for common metals are shown in Fig. 2(b). For common engineering metal bicrystals under a uniaxial σ^{E} perpendicular to the GB, the variation of σ_{h} at a GB is 14% for aluminum, 54% for iron and nickel, and 78% for copper, when compared to an isotropic material. In alkali metals, F_{h} can take a negative value, indicating that dilatation in bulk can give rise to compression on one side of the GB and large tension on the other side. As both σ_{h} and its gradient [33] play significant roles in the segregation and diffusivity [32] of interstitial atomic species and poorly fitting substitutional atomic species, precipitation processes can be affected particularly in materials with large variations in F_{h} values.

Based on Eq. (21) and (24), IF is further simplified as

$$\begin{aligned} IF &\approx \frac{1/E^{\mathrm{I}}_{\mathrm{Y}} - 1/E^{\mathrm{II}}_{\mathrm{Y}}}{(F^{\mathrm{I}}_{22}+F^{\mathrm{II}}_{22})\chi+4s_{11}+4s_{12}} \\ &\approx \frac{6(1/E^{\mathrm{I}}_{\mathrm{Y}} - 1/E^{\mathrm{II}}_{\mathrm{Y}})}{10s_{11}+14s_{12}+s_{44}}, \end{aligned} \tag{29}$$

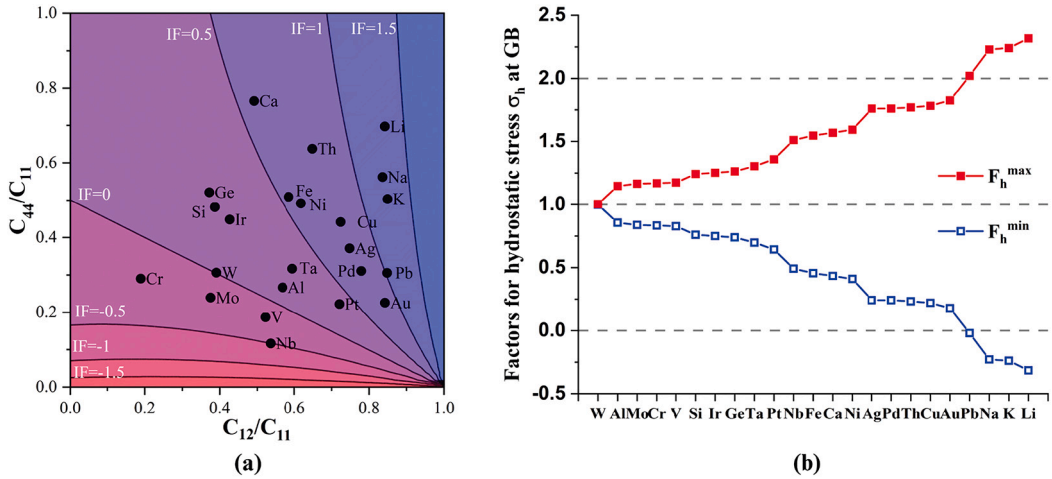

Fig. 2. (Color online) (a) The relation between elastic components and incompatibility factor, according to Eq. (25). The positions of common metals are labeled with black solid circles. (b) The maximum and minimum stress concentration factor F_h for hydrostatic stress σ_h at GBs for common metals, according to Eq. (28).

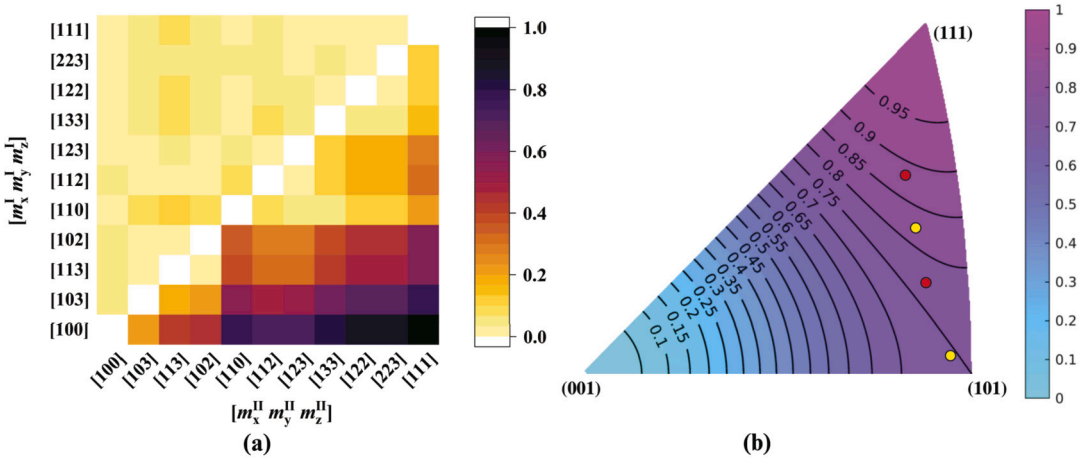

Fig. 3. (Color online) (a) For low-index GBs, IF^{GB} estimated by Eq. (32) are shown below the diagonal, while above the diagonal the maximum absolute value of IF^{GB} (exact) - IF^{GB} (Eq. (32)) that occurs when one of the two grains is rotated around the Y-axis is displayed. (b) Compliance factor as function of the grain orientation according to Eq. (31). The orientations of two bicrystals in [34] are presented by red dots for one bicrystal and yellow dots for another bicrystal.

where E_Y^I (E_Y^{II}) is the Young's modulus of grain I (II) along the global Y-axis. Here $(F_{22}^I + F_{22}^{II})\chi$ in the denominator is replaced by $-\frac{1}{3}\chi$ to ensure the accuracy of the approximation in predicting high absolute values of IF.

Eq. (29) disregards the stress variations arising from rotating the two grains around the direction of σ^E for two reasons. Firstly, IF, being defined as sum of σ_1/σ^E and σ_3/σ^E, is less sensitive to variations of individual stress components. Secondly, the bicrystal structure displays at least a four-fold symmetry during the rotation around global Y-axis. This equation is in good agreement with the analytical results (see Supplement C). Hence, while $\boldsymbol{m}^I$ and $\boldsymbol{m}^{II}$ have a strong influence on IF, the other four Miller indices have little effect. Therefore, the GB in the bicrystal model can be characterized by $\boldsymbol{m}^I$ and $\boldsymbol{m}^{II}$.

In order to clarify the role of the orientations of the two grains, we define a rescaled incompatibility factor for GBs

$$IF^{GB} = IF/IF^{max}, \tag{30}$$

ranging from -1 to 1, which is independent of the elastic anisotropy. The IF^{GB} for low-index GBs are shown in Fig. 3(a).

For general GBs, it is convenient to define the compliance factor (CF) to separate the contributions to IF^{GB} from each grain. For grain I,

$$\begin{aligned} CF^I &= \frac{1/E^{min} - 1/E_Y^I}{1/E^{min} - 1/E^{max}} \\ &= -3F_{22}^I \\ &= 3\left((m_x^I m_y^I)^2 + (m_x^I m_z^I)^2 + (m_y^I m_z^I)^2\right), \end{aligned} \tag{31}$$

where E^{min}, E^{max} are the minimum and maximum Young's modulus for the material, and analogous for grain II. Then IF^{GB} is expressed as

$$IF^{GB} = CF^{II} - CF^I. \tag{32}$$

Fig. 3(b) shows a contour plot of CF as function of $\boldsymbol{m}$ of each grain in a (0 0 1) inverse pole figure. This figure displays two important features.

First, the geometry of each GB can be presented as two points, corresponding to grain I and grain II, in Fig. 3(b). Then the rescaled IF for a given GB can be read from the map according to Eq. (32), e.g. the maximum of IF^{GB}, at 1, corresponds to $\boldsymbol{m}^I$, $\boldsymbol{m}^{II}$ parallel to [1 0 0] and [1 1 1], respectively.

Second, the IF for GBs with large misorientation is not always large. The IF vanishes for two grains with orientations located along a contour line. Therefore, even for materials with high anisotropy, it is possible to design textures with near-zero stress incompatibility at GBs.

Considering the proportional relationship between IF and $[\sigma_h]$ shown in Eq. (21), Fig. 3 is also valid for estimating the magnitude of $[\sigma_h]$ for various GBs.

In recent in-situ tensile tests of bicrystals [34], the orientations of grains at both sides of GBs are represented by pairs of dots in Fig. 3(b). The corresponding IF^{GB} is approximately 0.1. This implies that the stress incompatibility in the experiments are only 1/10 of the most extreme configuration. This may explain why the initial fracture position in the experiments did not occur at pre-existing GBs [34].

In summary, we have quantified incompatibility factor $IF = (\sigma_1 + \sigma_3)/\sigma^E$ and the discontinuity in hydrostatic stress σ_h near grain boundaries under external stress σ^E with a bicrystal model. The extreme values have been derived in terms of elastic tensor components. The incompatibility factors for general grain boundaries are estimated based on grain orientations. These findings provide valuable insights into failure phenomena, such as creep and fatigue, that occur in polycrystalline materials. Moreover, identifying grain boundaries with high and low stress concentration can guide the design of higher-performing materials.

Declaration of competing interest

The authors declare that they have no known competing financial interests or personal relationships that could have appeared to influence the work reported in this paper.

Acknowledgements

The authors gratefully acknowledge financial support from China Scholarship Council (CSC, No. 202006120016). The authors would like to thank ir. Jan Steven Van Dokkum and Prof. Leo Kestens for helpful discussions.

Appendix A. Supplementary material

Supplementary material related to this article can be found online at https://doi.org/10.1016/j.scriptamat.2023.115570.

References

[1] B. Schonfelder, D. Wolf, S. Phillpot, M. Furtkamp, Molecular-dynamics method for the simulation of grain-boundary migration, Interface Sci. 5 (1997) 245–262.
[2] M. Tonks, P. Millett, W. Cai, D. Wolf, Analysis of the elastic strain energy driving force for grain boundary migration using phase field simulation, Scr. Mater. 63 (2010) 1049–1052, https://doi.org/10.1016/j.scriptamat.2010.07.034.
[3] P. Lejcek, S. Hofmann, Thermodynamics and structural aspects of grain boundary segregation, Crit. Rev. Solid State Mater. Sci. 20 (1995) 1–85, https://doi.org/10.1080/10408439508243544.
[4] S.J. Fensin, J.P. Escobedo-Diaz, C. Brandl, E.K. Cerreta, G.T. Gray, T.C. Germann, S.M. Valone, Effect of loading direction on grain boundary failure under shock loading, Acta Mater. 64 (2014) 113–122, https://doi.org/10.1016/j.actamat.2013.11.026.
[5] N.J. Teng, T.H. Lin, Elastic anisotropy effect of crystals on polycrystal fatigue crack initiation, J. Eng. Mater. Technol. 117 (1995) 470–477, https://doi.org/10.1115/1.2804741.
[6] F. Lu, Z. Guang, Z. Ke-shi, Grain boundary effects on the inelastic deformation behavior of bicrystals, Mater. Sci. Eng. A 361 (2003) 83–92, https://doi.org/10.1016/S0921-5093(03)00476-3.
[7] L.L. Li, P. Zhang, Z.J. Zhang, Z.F. Zhang, Effect of crystallographic orientation and grain boundary character on fatigue cracking behaviors of coaxial copper bicrystals, Acta Mater. 61 (2013) 425–438, https://doi.org/10.1016/j.actamat.2012.08.045.
[8] D.C. Crawford, G.S. Was, The role of grain boundary misorientation in intergranular cracking of Ni-16Cr-9Fe in 360 °C argon and high-purity water, Metall. Mater. Trans. A 23 (1992) 1195–1206, https://doi.org/10.1007/BF02665051.
[9] Y. Wei, A.F. Bower, H. Gao, Recoverable creep deformation and transient local stress concentration due to heterogeneous grain-boundary diffusion and sliding in polycrystalline solids, J. Mech. Phys. Solids 56 (2008) 1460–1483, https://doi.org/10.1016/j.jmps.2007.08.007.
[10] M.E. Kassner, M.T. Pérez-Prado, Five-power-law creep in single phase metals and alloys, Prog. Mater. Sci. 45 (2000) 1–102, https://doi.org/10.1016/S0079-6425(99)00006-7.
[11] B. Chen, P.E. Flewitt, A.C. Cocks, D.J. Smith, A review of the changes of internal state related to high temperature creep of polycrystalline metals and alloys, Int. Mater. Rev. 60 (2015) 1–29, https://doi.org/10.1179/1743280414Y.0000000041.
[12] V. Randle, Grain boundary engineering: an overview after 25 years, Mater. Sci. Technol. 26 (2010) 253–261, https://doi.org/10.1179/026708309X12601952777747.
[13] J. Sidor, A. Miroux, R. Petrov, L. Kestens, Microstructural and crystallographic aspects of conventional and asymmetric rolling processes, Acta Mater. 56 (2008) 2495–2507.
[14] K.A. Sofinowski, S. Raman, X. Wang, B. Gaskey, M. Seita, Layer-wise engineering of grain orientation (lego) in laser powder bed fusion of stainless steel 316L, Addit. Manuf. 38 (2021) 101809, https://doi.org/10.1016/j.addma.2020.101809.
[15] J. Hou, R. Li, Q. Wang, H. Yu, Z. Zhang, Q. Chen, H. Ma, X. Wu, X. Li, Z. Zhang, Breaking the trade-off relation of strength and electrical conductivity in pure al wire by controlling texture and grain boundary, J. Alloys Compd. 769 (2018) 96–109.
[16] L. Kestens, H. Pirgazi, Texture formation in metal alloys with cubic crystal structures, Mater. Sci. Technol. 32 (2016) 1303–1315.
[17] P. Peralta, L. Llanes, J. Bassani, C. Laird, Deformation from twin-boundary stresses and the role of texture: application to fatigue, Philos. Mag. 70 (1994) 219–232, https://doi.org/10.1080/01418619408242547.
[18] S. Kumar, S.K. Kurtz, V.K. Agarwala, Micro-stress distribution within polycrystalline aggregate, Acta Mech. 114 (1996) 203–216, https://doi.org/10.1007/BF01170404.
[19] P. Peralta, C. Laird, Compatibility stresses in fatigued bicrystals: dependence on misorientation and small plastic deformations, Acta Mater. 45 (1997) 5129–5143, https://doi.org/10.1016/S1359-6454(97)00184-5.
[20] T. Richeton, S. Berbenni, Effects of heterogeneous elasticity coupled to plasticity on stresses and lattice rotations in bicrystals: a field dislocation mechanics viewpoint, Eur. J. Mech. A, Solids 37 (2013) 231–247, https://doi.org/10.1016/j.euromechsol.2012.06.010.
[21] T. Richeton, I. Tiba, S. Berbenni, O. Bouaziz, Analytical expressions of incompatibility stresses at $\Sigma3\langle111\rangle$ twin boundaries and consequences on single-slip promotion parallel to twin plane, Philos. Mag. 95 (2015) 12–31, https://doi.org/10.1080/14786435.2014.984787.
[22] I. Tiba, T. Richeton, C. Motz, H. Vehoff, S. Berbenni, Incompatibility stresses at grain boundaries in ni bicrystalline micropillars analyzed by an anisotropic model and slip activity, Acta Mater. 83 (2015) 227–238, https://doi.org/10.1016/j.actamat.2014.09.033.
[23] R. Ahluwalia, T. Lookman, A. Saxena, Elastic deformation of polycrystals, Phys. Rev. Lett. 91 (2003) 1–4, https://doi.org/10.1103/PhysRevLett.91.055501.
[24] Y. Zhao, R. Tryon, Automatic 3-d simulation and micro-stress distribution of polycrystalline metallic materials, Comput. Methods Appl. Mech. Eng. 193 (2004) 3919–3934, https://doi.org/10.1016/j.cma.2004.02.015.
[25] M. Kamaya, Y. Kawamura, T. Kitamura, Three-dimensional local stress analysis on grain boundaries in polycrystalline material, Int. J. Solids Struct. 44 (2007) 3267–3277, https://doi.org/10.1016/j.ijsolstr.2006.09.020.
[26] A. Fallahi, A. Ataee, Effects of crystal orientation on stress distribution near the triple junction in a tricrystal γ-TiAl, Mater. Sci. Eng. A 527 (18–19) (2010) 4576–4581.
[27] C. Gandhi, M.F. Ashby, Overview no. 5. fracture-mechanism maps for materials which cleave: F.C.C., B.C.C. and H.C.P. metals and ceramics, Acta Metall. 27 (1979) 1565–1602, https://doi.org/10.1016/0001-6160(79)90042-7, reference book for fracture type.
[28] M. Hayes, A. Shuvalov, On the extreme values of Young's modulus, the shear modulus, and Poisson's ratio for cubic materials a stress analysis method for bi-axially loaded fastener hole in composite laminate of finite geometry, J. Appl. Mech. 65 (1998) 786–787.
[29] E.A. Brandes, G.B. Brook, Smithells Metals Reference Book, Elsevier, 2013.
[30] N. Gunkelmann, H. Ledbetter, H.M. Urbassek, Experimental and atomistic study of the elastic properties of α' Fe-C martensite, Acta Mater. 60 (2012) 4901–4907, https://doi.org/10.1016/j.actamat.2012.05.038.
[31] V. Revi, S. Kasodariya, A. Talapatra, G. Pilania, A. Alankar, Machine learning elastic constants of multi-component alloys, Compos. Mater. Sci. 198 (10) (2021), https://doi.org/10.1016/j.commatsci.2021.110671.
[32] M. Werner, H. Mehrer, H.D. Hochheimer, Effect of hydrostatic pressure, temperature, and doping on self-diffusion in germanium, Phys. Rev. B 32 (6) (1985) 3930.
[33] H. Abdolvand, Progressive modelling and experimentation of hydrogen diffusion and precipitation in anisotropic polycrystals, Int. J. Plast. 116 (2019) 39–61.
[34] M.T. Kiani, L.T. Gan, R. Traylor, R. Yang, C.M. Barr, K. Hattar, J.A. Fan, X.W. Gu, In situ tem tensile testing of bicrystals with tailored misorientation angles, Acta Mater. 224 (2022) 117505, https://doi.org/10.1016/j.actamat.2021.117505.
[35] R.H. Wagoner, Calculating dislocation spacings in pile-ups at grain boundaries, Metall. Trans. A 12 (1981) 2015–2023.
[36] X.L. Chen, T. Richeton, C. Motz, S. Berbenni, Elastic fields due to dislocations in anisotropic bi- and tri-materials: applications to discrete dislocation pile-ups at grain boundaries, Int. J. Solids Struct. 164 (2019) 141–156.